FULL PAPER

Exploiting High-Performance Anode through Tuning the Character of Chemical Bonds for Li-Ion Batteries and Capacitors

*Chaofeng Liu, Changkun Zhang, Haoyu Fu, Xihui Nan, and Guozhong Cao**

A high-performance anode material, MnNCN, is synthesized through a facile and low-cost method. The relationship between electrochemical properties and chemical composition is explored on the scientific considerations that can provide an insight on designing expected materials. MnNCN with the long bonding length of 2.262 Å in Mn—N and weak electronegativity of 3.04 Pauling units in N leads to a lower charge/discharge potential than that of MnO owing to the character of chemical bonds transformed to covalent dominating from ionic dominating in MnO. Covalent character increases the ratio of sharing electrons that decreases the migration energy of electrons in electrochemical reaction, which enhances the reactive reversibility and stability of electrode material. MnNCN delivered a reversibly specific capacity of 385 mA h g^{-1} at 5 A g^{-1} in a Li-ion half cell. Besides, a Li-ion hybrid capacitor with a high voltage of 4 V presents energy and power densities of respective 103 Wh kg^{-1} and 8533 W kg^{-1} and cycles at 5 A g^{-1} without detectable degradation after 5000 cycles.

1. Introduction

Energy and environmental issues are arguably becoming the foremost challenges in this century; harvesting and utilizing green energy have attracted increasing attention with great efforts being devoted to the exploration of new materials and/or efficient devices to meet the imperative demands in our modern life.[1–5] Supercapacitors possess high power density with extremely long cycling life;[6,7] however, they are limited by relatively low energy density in spite of various efforts in modifying microstructures and chemical compositions.[8,9] Secondary batteries, the most popular electric energy storage devices with high energy density, work on reversible redox reactions to convert chemical potential to electric energy and have been widely used to power portable electronics and electric vehicles.[10–13] As the key components, cathodes and anodes determine the working voltage and energy density of batteries. While a high capacity is desired in both electrodes, a high potential in cathode and a low potential in anode are needed for a wide working voltage of batteries within the safe operating range of electrolyte.[14–16] Similar to cathodes, anodes work through three mechanisms: intercalation, conversion, and alloying,[17] thus, it is not surprised that transition metal oxides and complex oxides, metals and lithiation compounds have been studied intensively over the past years.[17–21] For example, intercalation compounds, such as $Li_4Ti_5O_{12}$, can insert and extract Li ion from the crystal lattices reversibly with a small strain offering a highly stable cyclability and an ideal potential plateau,[22] but deliver a relatively low specific capacity of 175 mA h g^{-1}.[23,24] Metals and metalloids including Sn, Zn, Pb, Bi, Se, and Si are based on alloying mechanism to store charges and ions, offering exceedingly high specific storage capacity but accompanied with drastic volume change during lithiation/delithiation leading to inferior cyclability.[25–29] Transition metal oxides, such as Mn—O, Fe—O, Co—O, Ni—O, and Cu—O, store charges through reversible conversion reactions, in which metal oxides decompose to metal and Li_2O and display a high specific capacity. However, such metal oxides also suffer from poor cycling stability.[19,30–33] Transition metal nitrides and fluorides have also been studied and demonstrated the capability of reversible conversion reactions but also suffer from the similarly inferior cyclability.[34–36] To circumvent the challenges in conversion materials, design and fabrication of various nano and microstructures, or doping with heteroatoms have been investigated with some noticeable improvement.[37–40] Exploring new materials with desired properties based on some fundamental considerations is another effective approach. For example, tuning the covalent-ionic bond characters between ion components can effectively alter the electrochemical potential of electrode materials.[41] The present investigation has explored a new anode material, manganese carbodiimide (MnNCN) with excellent lithium storage properties. **Figure 1**a is the schematic illustrating the crystal structure of MnNCN that consists of alternating layers of Mn^{2+} cations and NCN^{2-} anions (the pseudo-sulfide anions) along the trigonal axis, and the anions are strictly linearly oriented perpendicular to the layers. Each divalent Mn ion is coordinated by six nitrogen atoms and the

Dr. C. Liu, Dr. C. Zhang, H. Fu, X. Nan, Prof. G. Cao
Beijing Institute of Nanoenergy and Nanosystems
Chinese Academy of Sciences
Beijing 100083, China
E-mail: gzcao@u.washington.edu
Prof. G. Cao
Department of Materials Science and Engineering
University of Washington
Seattle, WA 98195, USA

DOI: 10.1002/aenm.201601127

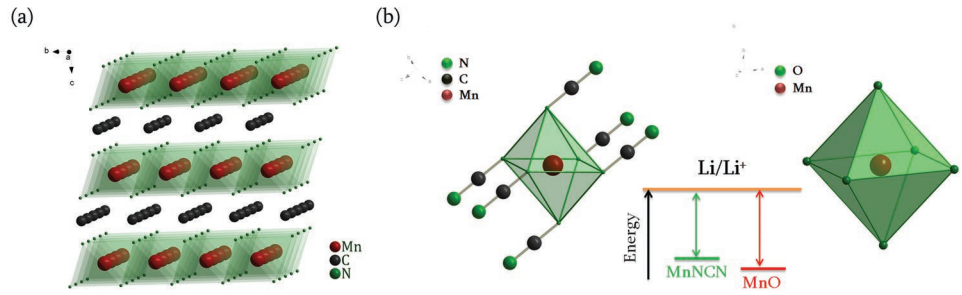

Figure 1. a) Crystal structure of MnNCN. Mn ions are coordinated by six N ions to form octahedrons, and the carbon atoms fill the gaps between MnN_6 layers for connecting the N atoms in alternating layers. b) The coordination of center metal ions and the energy level between MnO and MnNCN. MnNCN has a larger degree of covalent bonding than MnO and has an increased energy level related to charge transfer during the process of electrochemical reaction,[15,44] because C and N have the weaker Pauling electronegativity of respective 2.55 and 3.04 Pauling units, but O renders a higher value of 3.44 Pauling units.

bonding length of Mn—N is 2.262(2) Å that deviates from the predicted 2.29 Å based on the effective ionic radii[42] and 2.28 Å on bond-valence calculations.[43] The resulting octahedron around Mn^{2+} is slightly squeezed with the angle between N–Mn–N of 95.9(1)° and 84.1 (1)° and the shortest Mn^{2+}-Mn^{2+} distance is 3.358(4) Å.[44] In comparison, in a simple cubic MnO crystal, the distances between Mn—O and Mn—Mn are 2.222(5) and 3.142(4) Å, respectively. Both Mn and O have six coordination ligands for each other. In addition, the Pauling electronegativity of C, N, and O are 2.55, 3.04, and 3.44 Pauling units,[45] respectively. From these parameters, it is found that Mn^{2+} encompassed NCN^{2-} rather than O^{2-} in MnNCN, and the longer bonding length of Mn–N and the weaker Pauling electronegativity of N lead to a larger degree of covalent bonding and an increased energy level related to charge transfer in comparison with the characters of MnO during the process of electrochemical reaction (Figure 1b).[15,44] The increased energy level will be displayed as a lower potential plateau that benefits the device with a larger working voltage when MnNCN is used as anodes, in both batteries and capacitors, with high energy density. In the present study, a new anode material, MnNCN, with a high specific capacity of 725 mA h g^{-1} at 100 mA g^{-1} and an excellent cycling stability, and a Li-ion hybrid capacitor with a high voltage of 4 V with MnNCN anode and activated carbon (AC) cathode presented energy and power densities of respective 103 Wh kg^{-1} and 8533 W kg^{-1} without device optimization, and cycled at 5 A g^{-1} without detectable degradation after 5000 cycles, demonstrating an excellent cycling stability.

2. Results and Discussion

X-ray diffraction (XRD) pattern of the resulting sample from solvothermal synthesis shows the distinct characteristic peaks that confirm the product with a crystal structure (Figure S1a, Supporting Information); however, it did not match with any of the standard cards in the current crystal database. In order to understand the details of the structure, Fourier transform infrared spectroscopy (FT-IR) was used to collect the information of the bond vibration or stretch of the functional groups and the result is shown in **Figure 2**a. Weak N–H amines can be identified for melamine at 3413 and 3643 cm^{-1} and the absorbance at 3330 and 3190 cm^{-1} correspond to the stretch of secondary amine.[46,47] The C=N stretch and —C=N ring vibration show correspond to the absorbance bands for melamine compound at 1632 and 1530 cm^{-1}, respectively. The absorbance at 1182 cm^{-1} is attributed to aliphatic C—N vibration, and the absorption at 994 and 590 cm^{-1} corresponds to C—H out of plane deformation.[46,48] These results imply that the solvothermal grown product consists of groups: C=N, N—H, and C—N that contained in the raw materials. Differential scanning calorimetry/thermogravimetry (DSC/TG) was adopted to analyze the chemical or physical transformation during the heat treatment in nitrogen gas and the curves are shown in Figure 2b. An endothermic peak appeared at ≈380 °C accompanying with a drastic weight loss, indicating that a decomposition of solvothermal product. The XRD pattern of the sample calcined at 400 °C displays an amorphous state (Figure S1b, Supporting Information), but the sample will partially melt if the temperature exceeds 600 °C. Therefore, the solvothermal product was calcined at 500 °C for 120 min with a flowing nitrogen gas for ensuring the complete phase transformation. The phase of the sample calcined at 500 °C is coincident with the standard peaks of MnNCN (Figure 2c). More importantly, one issue is that the peak (012) is the strongest in the standard card; however, in the present study, the peak (003) has the highest intensity, implying that a preferential growth may be occurred during the synthesis. Figure S1c (Supporting Information) shows the morphology of solvothermal sample without calcination, and the sample exhibited a 2D irregular platelet shape with a thickness of ≈100 nm that suggests a preferential growth occurred during the solvothermal process. Although the calcination at 500 °C partially damaged the 2D morphology to the irregular particles (Figure S1d, Supporting Information), the intrinsic preferential orientation was reserved in the calcined sample and that is reflected by the difference in XRD peak intensities. Transmission electron microscopy (TEM) image of the calcined sample (Figure 2d) also supports this hypothesis, though the sample is sensitive to electron beam irradiation and high resolution TEM images could not be obtained. X-ray energy dispersive spectroscopy (EDS) data were collected and all the constituent elements distributed homogeneously (Figure S2, Supporting Information), these are in good accord with the results of XRD. In addition, X-ray photoelectron spectroscopy (XPS) was conducted and Mn $2p_{3/2}$ and $2p_{1/2}$ main peaks have the satellite structure on the higher binding-energy

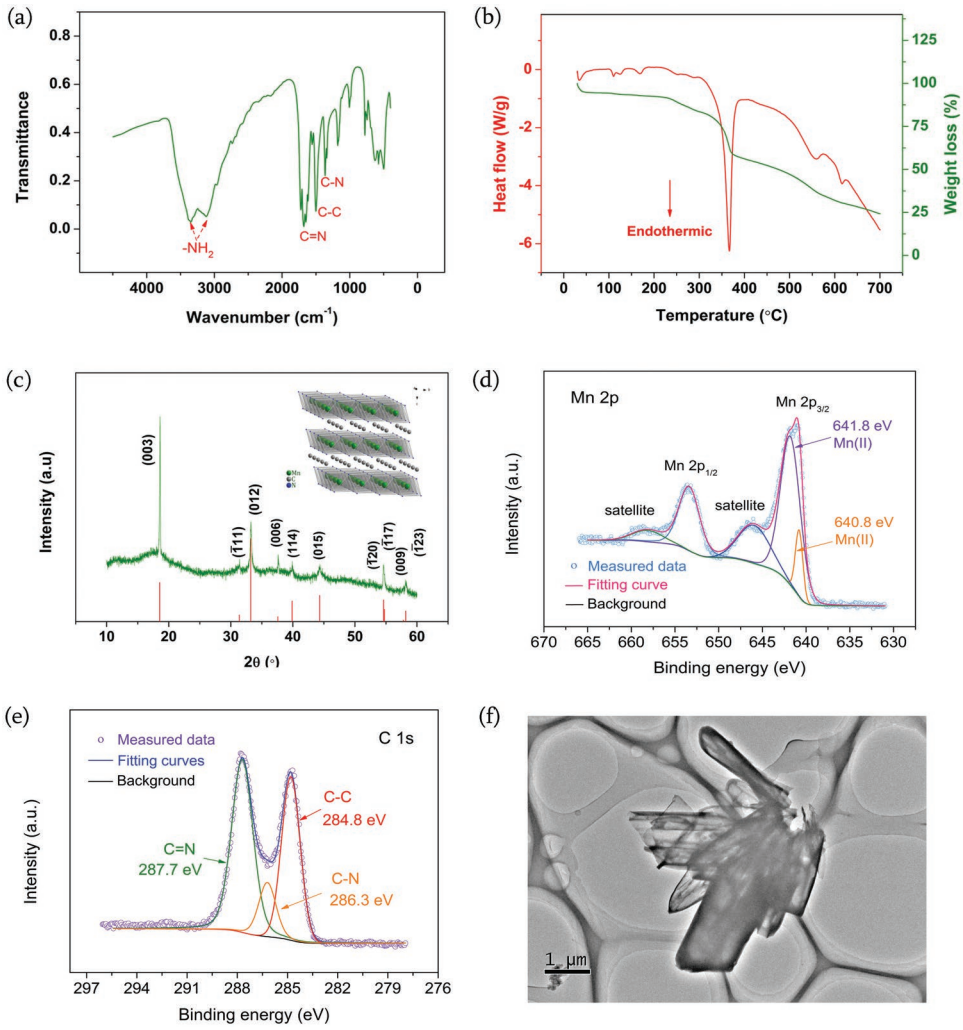

Figure 2. a) FT-IR spectrum of the precursor and the characteristic peaks relate to some unique functional groups which derived from the raw materials. b) DSC/TG curves of the precursor. An endothermic peak appears at 380 °C, indicating that a corresponding physical or chemical reaction occurred. c) XRD pattern of the calcined sample, the characteristic peaks are in perfect accordance with that of MnNCN. The standard peak positions were collected from the literature.[52] d) The Mn2p XPS spectra of MnNCN. e) The C1s XPS spectra of MnNCN. f) TEM image of calcined MnNCN sample.

sides, which indicates a strong Coulombic interaction between Mn 3*d* electrons and hybridization between Mn 3*d* and other valence orbitals.[49,50] Besides, the peak of C1s, at 284.8 eV, is assigned to sp^2 C-atoms, and the component at 286.3 eV usually attributes to C—N bonds and the component at 287.7 eV corresponds to C=N species.[51] All the results dovetail with the characters of bonds in MnNCN. Assuming the shape of the medium particle is a cuboid in Figure 2d, the length and width are 400 and 1000 nm, respectively. Since the specific surface area of 7.2 m^2 g^{-1} was determined from nitrogen sorption isotherm (Figure S3, Supporting Information) and the density of MnNCN is 3.38 cm^3 g^{-1}, the thickness of the cuboid crystal was calculated and found to be of ≈115 nm that agrees with the observed results from scanning electron microscope (SEM) or TEM. Apart from the morphologies and crystalline structure of resulting sample, it is worth noting that the synthesis method is also novel and simple because the method reported in literature was complex, in which a mixture of zinc carbodiimide and manganese(II) chloride was melted at 260 °C and subsequently the byproduct $ZnCl_2$ was sublimated at 500 °C through carefully controlling heating process.[52] In the present study, both the precursors and synthesis process are cheap and facile, which permits scale-up preparation.

The resulting MnNCN was used to fabricate an electrode and then assembled to a half cell with Li metal as the counter electrode for electrochemical property characterization and measurements. **Figure 3**a shows the cyclic voltammogram (CV) curves of the MnNCN anode in the Li-ion half-cell in the first three cycles. In the first cathodic scan, one instinct peak appeared at 0.2 V, while a weak and broad peak was detected in the anodic scan within the voltage range of 0.8–1.5 V. In the subsequent 2nd and 3rd scans, two cycle curves overlapped and the cathodic and anodic peaks resided at 0.3 and 1.1 V, respectively, suggesting that the MnNCN electrode exhibits a good reversibility for lithium-ion insertion and extraction. In comparison with the CV curves of MnO (Figure S4a, Supporting Information), the cathodic potential of MnNCN at 0.30 V is lower than 0.35 V of MnO and the anodic potential of MnNCN

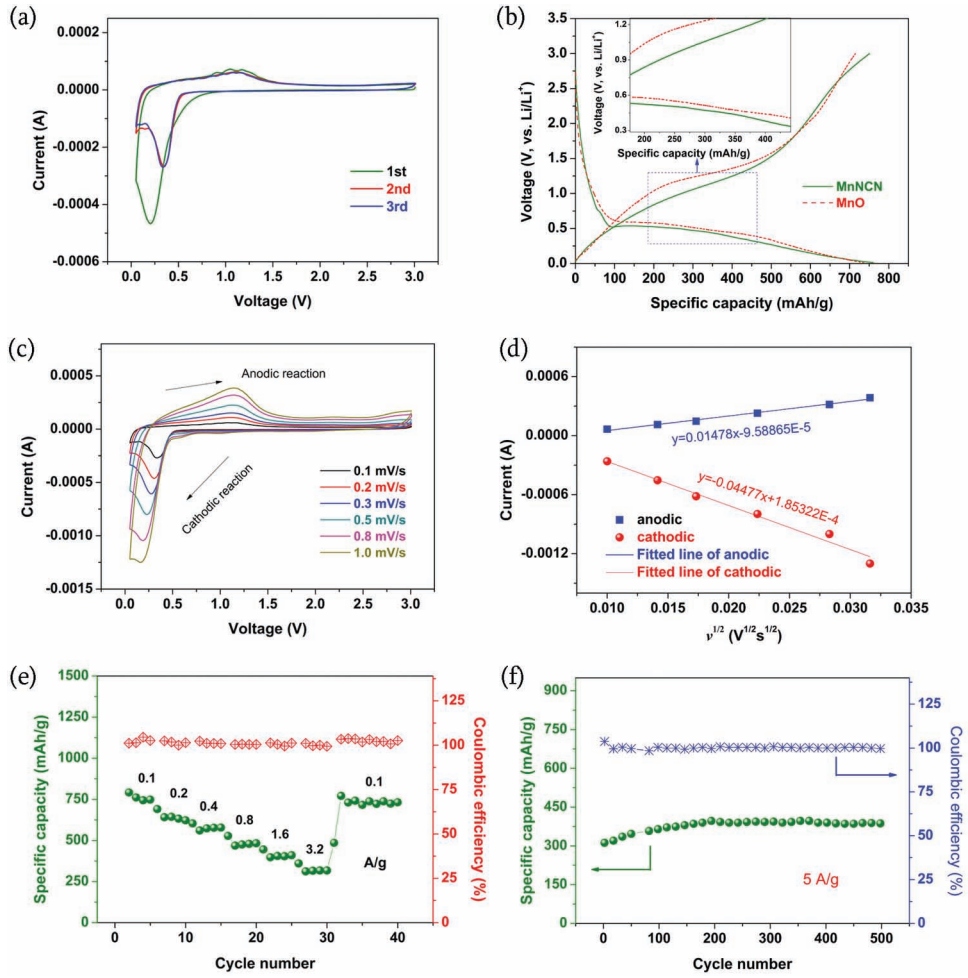

Figure 3. a) CV curves at 0.1 mV s^{-1}. The cathodic peak resides at 0.3 V and the anodic peak locates at 1.1 V, both differ from the characteristics of MnO. b) The charge/discharge profiles in MnNCN and MnO tested at 0.1 A g^{-1} in the 4th cycle that ensure the electrode material with a stable cycling state, the positions of potential profiles support the arguments from crystal field theory. The inset enlarges the difference between the charge/discharge profiles of both anodes. c) CVs curves measured at various current densities and the deviations in redox peaks indicate the polarization. d) Relationship between peak currents and scanning rates. The slope of the fitting linear can be used to evaluate the Li-ion diffusion coefficient. e) Rate performance measured with different current densities in the voltage potential of 0.01–3.00 V. f) Cycling stability tested at 5 A g^{-1}. The capacity increases the cycling number and stabilizes after 200 cycles.

at 1.1 V is lower than 1.25 V of MnO. Such a shift of cathodic and anodic potentials stems from the change of energy level as illustrated in Figure 1. Mn—N bond has a length of 2.226 Å longer than 2.222 Å of Mn—O, and N has a Pauling electronegativity of 3.04 weaker than 3.44 Pauling units of O element. Based on the electronegativity values, the character of chemical bonds can be evaluated through the following equation[53]

$$\%\text{covalent character} = 100 \times \exp[-0.25(X_a - X_b)^2] \quad (1)$$

where X_a and X_b are the electronegativity value of anion and cation, respectively. The electronegativity value of Mn is 1.55 Pauling units. Thus, the ratio of covalent bonds in MnO approximates to 40.9%, and the ratio in MnNCN reaches 57.4%, implying that MnNCN has a high degree of covalency and the electrons in 3*d* orbitals possess higher energy. Combined longer bond and small electronegativity lead to a weaker attraction to electrons in 3*d* orbitals of Mn^{2+} in MnNCN, thus a less energy is required to extract the electrons in anodic process, leading to a lower anodic potential based on the Nernst equation[15]

$$\Delta G = -nEF \quad (2)$$

where ΔG, n, E, and F stand for Gibbs energy difference, electron number, electrochemical potential, and Faraday constant, respectively. In the reverse process, the energy released in the cathodic process was also smaller compared with that in MnO due to the e_g orbitals has higher energy in MnNCN. These agree well with the crystal field theory, weaker interactions between center ions and coordination ligands correspond to smaller splitting in 3*d* of Mn^{2+}, and a lower electrochemical potential displays in electrode materials.[15,54] The charge/discharge profiles shown in Figure 3b further support the above explanation; MnNCN exhibits a lower potential than that in MnO, albeit the difference is small. The less significant difference in potential

profiles is reasonable considering the fact that the potential is determined by the order of electron extraction and insertion in orbitals as described in MnO.[55] Mn is a many-electron atom with the electronic configuration of [Ar]$3d^5 4s^2$. When oxidized from Mn^0 to Mn^{2+} such as in the formation of MnO, 4*s* orbital loses the electrons first because the overlapping electrons cloud in 3*d* and 4*s* orbitals. Then, anions coordinate with Mn^{2+} to form octahedron that induces the 3*d* orbital splitting to form t_{2g} and e_g orbitals with a high spin state. At the same time, the splitting leads to the electrons hopping from e_g to 4*s* because e_g has the higher energy level.[54] The continuous electrons hopping is accompanied with a continuous energy change that results in the sloping charge curve. During the reduction, the incoming electrons jump to e_g orbital to reduce the overall energy. The same energy level of both e_g orbitals causes the equivalent energy change in the discharge process, displaying a discharge potential plateau.[56] The energy difference of electrons hopping in *d* (or *f* orbitals) determines the electrochemical potentials of electrode materials.[57,58] The electronic structure and available valence states of Mn-compound endows it a valuable discharge voltage plateau. Figure 3c compares the CVs at various scanning rates from 0.1 to 1.0 mV s^{-1}. With increased scanning rates, the cathodic peak displayed a slight shift towards lower potential, attributable to the polarization as reported widely in electrode materials.[59] The peak current densities in cathodic and anodic scans at different scanning rates are used to calculate the Li-ion diffusion coefficient; the apparent diffusion coefficients of Li ions in MnNCN were calculated based on the Randles–Sevchik equation[60]

$$I_p = 0.4463\left(\frac{F^3}{RT}\right)^{1/2} n^{3/2} A D^{1/2} C_0 v^{1/2} \quad (3)$$

where I_p is the peak current (A), *R* is the gas constant (8.314 J mol^{-1} K^{-1}), *T* (K) is the absolute temperature, *F* is the Faraday constant (96 500 C mol^{-1}), *n* is the number of electrons transferred per molecule (2), *A* is the active surface area of the electrode (0.50 cm^2), C_0 is the concentration of Li ions in the electrolyte (1.0×10^{-3} mol cm^{-3}), *D* is the apparent ion diffusion coefficient (cm^2 s^{-1}), and *v* is the scanning rate (V s^{-1}). From the slopes of the fitting lines collected from peak current densities (I_{pa}) (Figure 3d), the apparent diffusion coefficients, *D*, of MnNCN are 1.51×10^{-9} and 1.39×10^{-8} cm^2 s^{-1} for anodic and cathodic processes, respectively. These coefficients are more than one order of magnitude larger than 4.96×10^{-10} and 7.07×10^{-9} cm^2 s^{-1} of MnO, respectively (Figure S4b, Supporting Information). The difference in diffusion coefficients is originated from the weaker interactions betwwen cations and anions and longer bonding length between Mn—N in comparision with the corresponding characters in MnO, because the weaker electronegativity in N than O. The anions in the crystal lattice with weak attraction to Li ions would lead to a superior diffusion coefficient in MnNCN. Figure 3e shows the rate capability of MnNCN in the voltage window of 0.01–3.00 V. In the initial cycles, MnNCN electrode delivered a discharge capacity of 1534 mA h g^{-1} (not included in the figure for better presentation of other data) at a current density of 0.1 A g^{-1}, but the charge capacity was only 792 mA h g^{-1}. The difference is likely stemmed from Li-ion exhaustion in the formation of solid electrolyte interphase (SEI).[61,62] In the rate performance tests, MnNCN was measured at different current densities ranging from 0.2 to 3.2 A g^{-1} and the delivered capacities varied inversely between 650 and 331 mA h g^{-1}. The capacity was restored to 725 mA h g^{-1} when the current density was reduced to 0.1 A g^{-1}, indicative of an excellent rate capability of MnNCN. The long-term cyclability was studied in the half cell and the current density was set at 5 A g^{-1}. Every cycle could be completed in 9 min and the initial capacity was 308 mA h g^{-1}. The capacity increased initially with the cycling number till 200 cycles and then stabilized at 385 mA h g^{-1} thereafter. The initial increase of capacity might have derived from the reversible polymeric gel-like film formed on the surface of MnNCN particles similar to that verified in MnO or other anodes.[61,63–65] It should be noted that the discharge capacity of 385 mA h g^{-1} at 5 A g^{-1} is higher than that of other manganese compounds even combined with graphene, such as MnO/graphene[66] and $MnCO_3$/graphene[67] composites under the same current density, and the displayed excellent cycling stability, much better in comparison with the reported conversion materials.[39,68] In addition, the electrochemical impedance spectra of the cells were collected before and after cycles (Figure S5, Supporting Information), the charge transfer resistance did not increase, even with a little decrease, demonstrating a stable electrochemical performance in MnNCN anode.

To detect the phase transition of MnNCN in the process of electrochemical reaction, ex situ XRD patterns were collected and compared at different charge/discharge states. Before the XRD analyses, the MnNCN electrodes were discharged and charged for three cycles in the potential window of 0.01–3.00 V at a rate of 0.1 A g^{-1} to ensure the electrode materials in a stable electrochemical state. Thus, the XRD patterns, in fact, were collected from the fourth cycle. The half cells were dissembled and the electrodes were taken out and washed by DMC first to remove the residual electrolyte or excess salts, and then dried at 120 °C for 12 h in vacuum. **Figure 4**a shows the XRD patterns of electrodes at different charge/discharge states, and the phase evolution can be followed in the process of electrode reactions. The characteristic peak (003) of MnNCN crystal was unambiguously identified in the pristine electrode, and the intensities of the peaks decreased during the discharge process and vanished at 0.01 V. While the vanished peaks appeared again and the peaks intensities became increasingly stronger as the charge proceeded. The reversible phase transition suggests that the electrode material MnNCN has an excellent reversibility as Li-ion anode. The phase transition presents the similarity with transition metal oxides[19] and the reaction mechanism can be considered as conversion reaction similar to that in MnO[69,70] possibly described with the following:

$$MnNCN + 2Li^+ + 2e^- \leftrightarrow Mn + Li_2NCN \quad (4)$$

Metallic Mn was precipitated in the discharge process but it was not found in the XRD patterns, probably due to the fact that the resulting Mn has a smaller crystallites or amorphous state so that it was reflected as the broad peak in the XRD patterns.[19] TEM image (Figure 4b) shows the sample with plate-like shape at the discharge state of 0.01 V, implying the 2D microstructure of pristine MnNCN crystals retained, regardless the change of

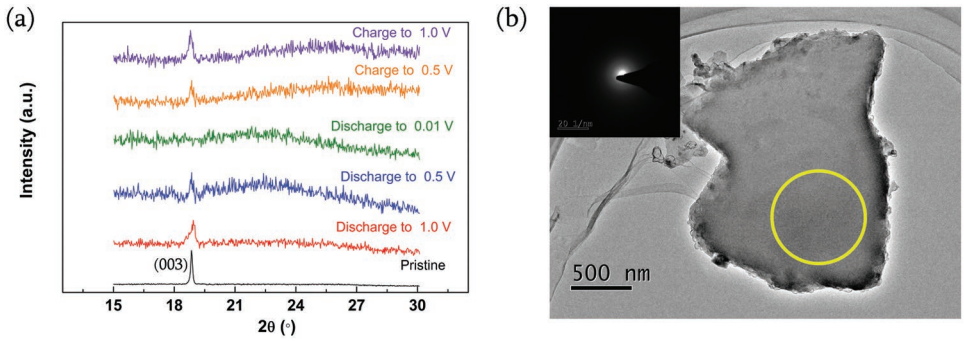

Figure 4. a) XRD patterns of electrodes at different charge/discharge states. The pristine sample shows the sharp characteristic peaks, the intensities of peaks decrease during the discharge process and the pattern presents an amorphous character at the full discharge state, while the intensities become stronger in the charge process. The change in peaks intensities implies the sample with an excellent reversibility. b) TEM image and SAED pattern of the sample with a discharge state of 0.01 V, the amorphous character is in accord with the results shown the XRD pattern of 0.01 V.

chemical composition and phase change through conversion reaction. The selected area electron diffraction (SAED) pattern in the inset of Figure 4b collected from the yellow circle zone exhibited an amorphous character that is in accord with the XRD pattern (0.01 V) shown in Figure 4a; the similar results were observed and reported in other conversion materials.[71] The experimental results strongly suggest that MnNCN stores lithium ions through a conversion reaction and displays a high specific capacity and an excellent cycling stability in Li-ion half cells. The excellent cycling stability might be attributable to the extremely small Mn particles with large surface area and thus large surface energy permitting an easy and reversible phase transition. Besides, the high degree of covalency suggests a high degree of sharing electrons in the chemical bonds and the weaker interaction between cations and anions, resulting in a high reversibility of material during the electrochemical reaction.

Apart from the electrochemical properties in Li-ion half cells, MnNCN anode was studied further in Li-ion hybrid capacitors with AC as cathode. The AC has a specific surface area of 1800 m^2 g^{-1}, which was used in other reports[72,73] and its rate capability is shown in Figure S6 (Supporting Information). The active mass ratio was set at 1:5 between anode and cathode to ensure the charge balance in both electrodes. Because of the lower average working potential at 0.3 V (vs Li/Li^+) of MnNCN anode and the highest potential to 4.5 V (vs Li/Li^+) for AC, the Li-ion hybrid capacitor based on MnNCN anode and AC would work with a high voltage of 4 V, as the case of MnO-based Li-ion capacitors.[55] **Figure 5**a shows the time–voltage curves of the capacitor at various current densities, and the curve profiles presented the characteristics of a pseudocapacitor, implying that the design and fabrication are reasonable. The rate capability was measured with various current densities at the working voltage window (Figure 5b), and the discharge capacities are 276, 263, 235, 198, 153, 103, 55, and 37 mA h g^{-1} at 0.2, 0.4, 0.8 1.6, 3.2, 6.4, 12.8, and 25.6 A g^{-1}, respectively. Besides, SEI growth stabilizes and Coulombic efficiency consequently increases with cycling to some steady-state value, but there is no Li-ion exhaustion, similar to what has been observed in half cells characterization. The capacitor was cycled at 5 A g^{-1} for 5000 cycles with the specific capacity maintained at ≈150 mA h g^{-1}, and displayed an undetected degradation in such a long-term cycling process (Figure 5c). This excellent cycling stability exhibits strong competitive advantage in comparison with Fe_3O_4/G//3D graphene[74] or 3D-MnO//CNS[75] Li-ion capacitors. More importantly, the specific capacity at the initial cycles increases with the cycle number; this phenomenon can be attributed to two possible reasons. One stems from the materials activation in the internal of particles as seen in Figure 3f, when the ions migrate to or electrolyte contacts the new surface of electrode as cracks form on the particle surface with the cycles, similar to the verified results reported in NiO anode.[76] Another possibility may originate from the reversible decomposition of electrolyte with the formation of SEI and extra Li-ion adsorption/desorption on SEI contributing to the high experimental capacity[77] as suggested by the increasing coulombic efficiency at the first several cycles, and this uniform SEI is beneficial as it reduces the over-potential and concentration polarization.[57] Figure 5d is the Ragone plot of the MnNCN// AC capacitor showing the relationship between energy and power densities, and the maximum energy and power densities of 103 Wh kg^{-1} and 8533 W kg^{-1}, respectively, without any device optimization. The engineering the materials and device to optimize the lithium storage property and performance would further enhance both energy and power densities of the capacitor, as the mass ratio on both electrodes has different optimal values and is dependent on output performance in energy or power densities. Compared with both aqueous capacitors (MnO_2//CNT[78] and Graphene// MGC[79]) and nonaqueous/organic capacitor (SAC//SAC[80] and G-LTO//G-SU[81]), this MnNCN-based hybrid capacitor unambiguously demonstrated both high energy and power densities. Not only does the study on MnNCN provide an insight and fundamental understanding on design and tailor the electrochemical potential of electrode, but also help to choose desirable electrode materials for Li-ion capacitor with high energy and power densities. The excellent performance of the Li-ion capacitors makes them perfect energy storage technology bridging the gaps between secondary batteries and supercapacitors with both high energy and power densities as well as excellent cycling stability.

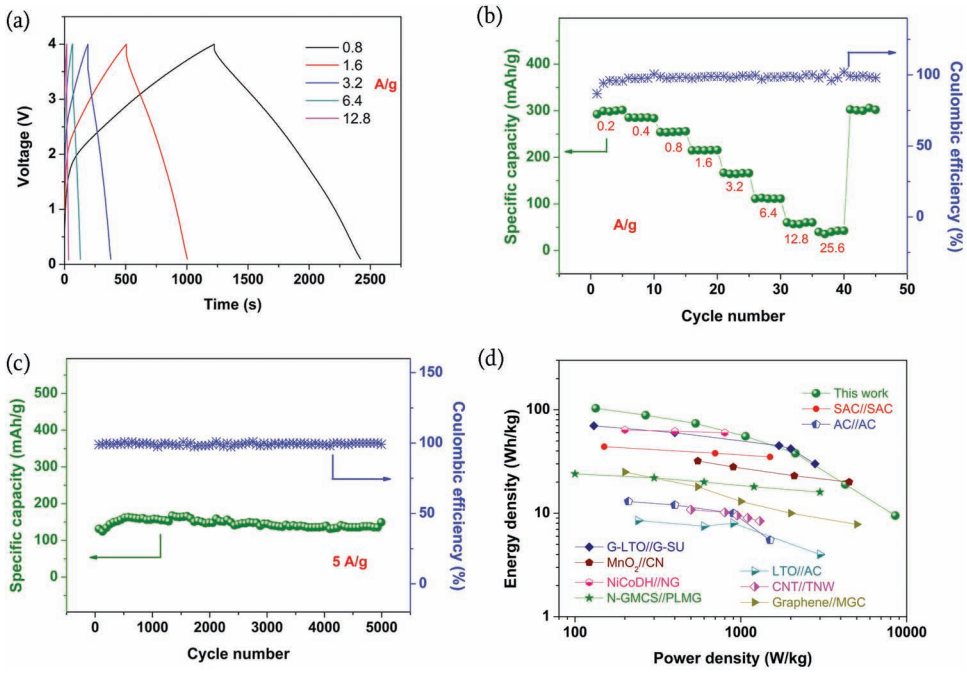

Figure 5. a) Voltage profiles of full capacitor in which MnNCN used as anode and AC as cathode. b) Rate performance of full capacitor measured with different current densities in the voltage potential of 0.10–4.00 V. c) Cycling stability tested at 5 A g^{-1}. d) Ragone plot of the full capacitor. The data calculated on the total active mass in both electrodes. The contrasting data collected from various systems, including G-LTO//G-SU,[81] SAC//SAC,[80] MnO_2//CNT,[78] Graphene//MGC,[79] AC//AC,[82] LTO//AC,[83] NiCoDH//NG,[84] N-GMCS//PLMG,[85] and CNT//TNW.[86]

3. Conclusions

A high-performance Li-ion anode, MnNCN, was synthesized through a facile solvothermal method with a following calcination. The long length of Mn—N bond and weak Pauling electronegativity of N endow high degree covalency of 57.4% in the chemical bonds in MnNCN, the covalent bonding leads to a decreased energy for electrons to be added to or extracted from 3*d* orbital of Mn^{2+} and makes a lower discharge potential in Li-ion batteries, which provides a golden rule for designing the desirable electrode materials with the expected electrochemical potential and the high reversibility and stability. MnNCN delivered a high reversible discharge capacity of 725 mA h g^{-1} at 0.1 A g^{-1} through conversion reaction with excellent rate capability and stable cycling performance. In addition, a high voltage capacitor built on MnNCN anode and activated carbon cathode demonstrated a high energy density of 103 Wh kg^{-1} and a high power density of 8533 W kg^{-1}. The Li-ion capacitor showed no detectable degradation after 5000 cycles at a rate of 5 A g^{-1}, suggesting a synergistic combination of high energy storage and large power supply bridging the gap between secondary batteries and supercapacitors.

4. Experimental Section

Synthesis: Melamine (0.25 g) was mixed with 70 mL octanoic acid and stirred at 600 RPM with 12 h to form a white solution, then 0.5 g $MnCl_2$ was added into the solution and continuously stirred at 500 RPM with 12 h. This process was carried out in the fume cupboard. The mixture was sealed into a 100 mL Teflon lined stainless steel and treated at 180 °C with 12 h. The product was washed and centrifuged by absolute alcohol three times and dried at 60 °C in an oven. At last, the obtained powder was calcined at 500 °C with 2 h with a flowing nitrogen gas of 100 SCCM, and the final product was a green powder.

Structural Characterization: The phases of samples were detected on a X-ray diffractometer (X'pert3 powder, Netherlands) with a Cu-Kα radiation source (λ = 1.54056 Å) and the scan step size was set at 0.013°. The microstructures of samples were observed by field-emission scanning electron microscope (HITACHI SU8200) at an accelerating voltage of 5 kV. DSC/TG instrument (Mettler-Toledo STAR system, DSC/TG) was used to study the pyrolysis temperature of the solvothermal sample with a flowing nitrogen of 50 mL min^{-1} and the heating rate was set at 10 °C min^{-1}. FT-IR (Bruker/VERTEX80v) with a resolution of 0.1 cm^{-1} was used to collect the information from the vibration or stretch of the functional groups in the solvothermal sample. The specific surface area was investigated using nitrogen sorption analyses via Micromeritics surface area and porosity analyzer (ASAP 2020 HD88, USA).

Capacitor Fabrication and Electrochemical Characterization: The electrochemical performances were investigated using 2032 coin cells. To prepare the working electrode, the slurry contained a mixture of MnNCN, carbon black, and carboxymethyl cellulose at a weight ratio of 70:20:10 was bladed on a Cu foil (thickness 10 µm, Shenzhen POXON Machinery Technology Co., LTD) with a setting thickness of 150 µm and then subjected to thermal treatment at 120 °C with 12 h in vacuum. The mass loading of the active material on each electrode disk was 1.0–1.5 mg cm^{-2}. The electrolyte was 1 M $LiPF_6$ in a 1:1:1 (vol%) mixture of ethylene carbonate, dimethyl carbonate, and diethyl carbonate, and a polypropylene film (Celgard 2400) was used as the separator. Li-ion capacitors were fabricated in which commercial activated carbon was employed as cathodes and MnNCN electrodes as anodes. In the process of capacitor fabrication, Celgard separator packaged porous Li metal foil was set between anode and cathode for separating both electrode and guaranteeing the sufficient Li sources in the electrochemical cycles as reported in reference.[55] The fabrication of cathodes are similar with

anodes but on an Al foil. Half cells were also assembled and lithium foil was used as the counter electrode for investigating the electrochemical properties of anode materials. All cells were assembled in an argon-filled glovebox where both the content of oxygen and water are below 0.5 ppm.

Galvanostatic charge–discharge tests of all cells were carried out on a Land CT2001A system (Wuhan, China) with various current densities. The operating voltage window for MnNCN, activated carbon half cells and Li-ion capacitors are 0.01–3.00 V (vs Li/Li^+), 2.0–4.5 V (vs Li/Li^+), and 0.1–4.0 V (MnNCN//AC), respectively. CVs were conducted on a Solartron SI 1287 at different scanning rate for characterizing the redox reaction of electrode materials in the process of charge/discharge. Electrochemical impedance spectroscopy were performed using the Solartron 1287A in conjunction with a Solartron 1260A impedance analyzer over the frequency range from 100 kHz to 0.01 Hz and the AC amplitude was 10.0 mV. The current densities for the half cells were calculated on the mass of active materials of electrodes and Li-ion capacitors were determined based on total mass of active materials on both electrodes. All electrochemical measurements were carried out at room temperature. The specific energy and specific power values of Li-ion capacitors were calculated as follows

$$P = I \times \Delta V / m$$
$$E = P \times t / 3600 \quad (5)$$
$$\Delta V = V_{max} - V_{min}$$

where I is the discharge current (A g^{-1}) and t is the discharge time (s), m is the total active mass on both electrodes (kg), V_{max} is the potential at the beginning of discharge after the IR drop, and V_{min} is the potential at the end of discharge.

Supporting Information

Supporting Information is available from the Wiley Online Library or from the author.

Acknowledgements

This work was partly supported by the "Thousands Talents" program for the pioneer researcher and his innovation team, China and also by the National Science Foundation (NSF, DMR 1505942). This work was also supported by the National Science Foundation of China (51374029) and (91433102), Program for New Century Excellent Talents in University (NCET-13-0668), and China Postdoctoral Science Foundation (2015M570987).

Received: May 29, 2016
Revised: July 12, 2016
Published online: September 9, 2016

[1] T. H. Kim, J. S. Park, S. K. Chang, S. Choi, J. H. Ryu, H. K. Song, *Adv. Energy Mater.* **2012**, *2*, 860.
[2] D. Larcher, J. M. Tarascon, *Nat. Chem.* **2015**, *7*, 19.
[3] J. Liu, *Adv. Funct. Mater.* **2013**, *23*, 924.
[4] M. S. Whittingham, *MRS Bull.* **2008**, *33*, 411.
[5] J. B. Goodenough, *Energy Storage Mater.* **2015**, *1*, 158.
[6] S. L. Candelaria, Y. Shao, W. Zhou, X. Li, J. Xiao, J. G. Zhang, Y. Wang, J. Liu, J. Li, G. Cao, *Nano Energy* **2012**, *1*, 195.
[7] P. Simon, Y. Gogotsi, *Nat Mater* **2008**, *7*, 845.
[8] S. L. Candelaria, G. Cao, *Sci. Bull.* **2015**, *60*, 1587.
[9] S. Candelaria, E. Uchaker, G. Cao, *Sci. China Mater.* **2015**, *58*, 521.
[10] M. M. Thackeray, C. Wolverton, E. D. Isaacs, *Energy Environ. Sci.* **2012**, *5*, 7854.
[11] R. Massé, E. Uchaker, G. Cao, *Sci. China Mater.* **2015**, *58*, 715.
[12] Y. Wang, R. Chen, T. Chen, H. Lv, G. Zhu, L. Ma, C. Wang, Z. Jin, J. Liu, *Energy Storage Mater.* **2016**, *4*, 103.
[13] S. Imtiaz, J. Zhang, Z. A. Zafar, S. Ji, T. Huang, J. A. Anderson, Z. Zhang, Y. Huang, *Sci. China Mater.* **2016**, *59*, 389.
[14] C. X. Zu, H. Li, *Energy Environ. Sci.* **2011**, *4*, 2614.
[15] C. Liu, Z. G. Neale, G. Cao, *Mater. Today* **2016**, *19*, 109.
[16] C. Liu, R. Massé, X. Nan, G. Cao, *Energy Storage Mater.* **2016**, *4*, 15.
[17] H. D. Yoo, E. Markevich, G. Salitra, D. Sharon, D. Aurbach, *Mater. Today* **2014**, *17*, 110.
[18] M. Zhang, T. Wang, G. Cao, *Int. Mater. Rev.* **2015**, *60*, 330.
[19] P. Poizot, S. Laruelle, S. Grugeon, L. Dupont, J. M. Tarascon, *Nature* **2000**, *407*, 496.
[20] V. Etacheri, R. Marom, R. Elazari, G. Salitra, D. Aurbach, *Energy Environ. Sci.* **2011**, *4*, 3243.
[21] M. Zhang, T. Zhang, Y. Ma, Y. Chen, *Energy Storage Mater.* **2016**, *4*, 1.
[22] T. F. Yi, S. Y. Yang, Y. Xie, *J. Mater. Chem. A* **2015**, *3*, 5750.
[23] L. Shen, E. Uchaker, X. Zhang, G. Cao, *Adv. Mater.* **2012**, *24*, 6502.
[24] L. Shen, C. Yuan, H. Luo, X. Zhang, S. Yang, X. Lu, *Nanoscale* **2011**, *3*, 572.
[25] M. N. Obrovac, V. L. Chevrier, *Chem. Rev.* **2014**, *114*, 11444.
[26] X. L. Wu, Y. G. Guo, L. J. Wan, *Chem. Asian J.* **2013**, *8*, 1948.
[27] X. Li, M. Gu, S. Hu, R. Kennard, P. Yan, X. Chen, C. Wang, M. J. Sailor, J. G. Zhang, J. Liu, *Nat. Commun.* **2014**, *5*, 4105.
[28] X. Zhou, Y. X. Yin, L. J. Wan, Y. G. Guo, *Chem. Commun.* **2012**, *48*, 2198.
[29] C. P. Yang, Y. X. Yin, Y. G. Guo, *J. Phys. Chem. Lett.* **2015**, *6*, 256.
[30] J. Cabana, L. Monconduit, D. Larcher, M. R. Palacín, *Adv. Mater.* **2010**, *22*, E170.
[31] R. Malini, U. Uma, T. Sheela, M. Ganesan, N. G. Renganathan, *Ionics* **2009**, *15*, 301.
[32] L. Song, S. Yang, W. Wei, P. Qu, M. Xu, Y. Liu, *Sci. Bull.* **2015**, *60*, 892.
[33] X. Hou, W. Zhang, X. Wang, S. Hu, C. Li, *Sci. Bull.* **2015**, *60*, 884.
[34] X. Xu, W. Liu, Y. Kim, J. Cho, *Nano Today* **2014**, *9*, 604.
[35] M. S. Balogun, W. Qiu, W. Wang, P. Fang, X. Lu, Y. Tong, *J. Mater. Chem. A* **2015**, *3*, 1364.
[36] H. Li, P. Balaya, J. Maier, *J. Electrochem. Soc.* **2004**, *151*, A1878.
[37] R. Liu, J. Duay, S. B. Lee, *Chem. Commun.* **2011**, *47*, 1384.
[38] E. Uchaker, G. Cao, *Chem. Asian J.* **2015**, *10*, 1608.
[39] J. Wang, H. Zhou, J. Nanda, P. V. Braun, *Chem. Mater.* **2015**, *27*, 2803.
[40] W. Li, L. Zeng, Y. Wu, Y. Yu, *Sci. China Mater.* **2016**, *59*, 287.
[41] B. C. Melot, J. M. Tarascon, *Acc. Chem. Res.* **2013**, *46*, 1226.
[42] R. Shannon, *Acta Crystallogr., Sect. A* **1976**, *32*, 751.
[43] N. E. Brese, M. O'Keeffe, *Acta Crystallogr., Sect. B* **1991**, *47*, 192.
[44] T. D. Boyko, R. J. Green, R. Dronskowski, A. Moewes, *J. Phys. Chem. C* **2013**, *117*, 12754.
[45] WebElements, http://www.webelements.com/electronegativity.html, accessed: June 2016.
[46] D. J. Merline, S. Vukusic, A. A. Abdala, *Polym. J.* **2013**, *45*, 413.
[47] N. E. Mircescu, M. Oltean, V. Chiş N. Leopold, *Vib. Spectrosc.* **2012**, *62*, 165.
[48] N. Yusof, S. Rahman, M. Hussein, N. Ibrahim, *Polymers* **2013**, *5*, 1215.
[49] D. Guo, Z. Wu, Y. An, X. Li, X. Guo, X. Chu, C. Sun, M. Lei, L. Li, L. Cao, P. Li, W. Tang, *J. Mater. Chem. C* **2015**, *3*, 1830.
[50] M. Meng, S. X. Wu, L. Z. Ren, W. Q. Zhou, Y. J. Wang, G. L. Wang, S. W. Li, *J. Appl. Phys.* **2014**, *116*, 173911.
[51] V. Leon, M. Quintana, M. A. Herrero, J. L. G. Fierro, A. d. l. Hoz, M. Prato, E. Vazquez, *Chem. Commun.* **2011**, *47*, 10936.
[52] X. H. Liu, M. Krott, P. Muller, C. H. Hu, H. Lueken, R. Dronskowski, *Inorg. Chem.* **2005**, *44*, 3001.

[53] W. D. Callister, *Fundamentals of Materials Science and Engineering*, John Wiley & Sons, Inc., New Jersey, USA **2001**.
[54] Z. D. Zhang, *Inorganic Chemistry,* Press of University of Science and Technology of China, China **2008**.
[55] C. Liu, C. Zhang, H. Song, C. Zhang, Y. Liu, X. Nan, G. Cao, *Nano Energy* **2016**, *22*, 290.
[56] R. Yazami, *High-Rate Li-Ion Intercalation in Nanocrystalline Cathode Materials for High-Power Li-Ion Batteries*, CRC Press, Ohio, USA, **2013**, Ch. 7, p. 227.
[57] J. K. Park, *Principles and Applications of Lithium Secondary Batteries*, Wiley-VCH, Germany **2012**.
[58] M. S. Islam, C. A. J. Fisher, *Chem. Soc. Rev.* **2014**, *43*, 185.
[59] E. Uchaker, H. Jin, P. Yi, G. Cao, *Chem. Mater.* **2015**, *27*, 7082.
[60] C. Zhang, H. Song, C. Liu, Y. Liu, C. Zhang, X. Nan, G. Cao, *Adv. Funct. Mater.* **2015**, *25*, 3497.
[61] S. Laruelle, S. Grugeon, P. Poizot, M. Dollé, L. Dupont, J. M. Tarascon, *J. Electrochem. Soc.* **2002**, *149*, A627.
[62] Y. Sun, X. Hu, W. Luo, Y. Huang, *J. Mater. Chem.* **2012**, *22*, 19190.
[63] Z. Xu, H. Wang, Z. Li, A. Kohandehghan, J. Ding, J. Chen, K. Cui, D. Mitlin, *J. Phys. Chem. C* **2014**, *118*, 18387.
[64] S. Grugeon, S. Laruelle, R. Herrera-Urbina, L. Dupont, P. Poizot, J. M. Tarascon, *J. Electrochem. Soc.* **2001**, *148*, A285.
[65] A. Ponrouch, P. L. Taberna, P. Simon, M. R. Palacín, *Electrochim. Acta* **2012**, *61*, 13.
[66] S. Zhang, L. Zhu, H. Song, X. Chen, J. Zhou, *Nano Energy* **2014**, *10*, 172.
[67] Y. Zhong, M. Yang, X. Zhou, Y. Luo, J. Wei, Z. Zhou, *Adv. Mater.* **2015**, *27*, 806.
[68] W. M. Zhang, X. L. Wu, J. S. Hu, Y. G. Guo, L. J. Wan, *Adv. Funct. Mater.* **2008**, *18*, 3941.
[69] H. Jiang, Y. Hu, S. Guo, C. Yan, P. S. Lee, C. Li, *ACS Nano* **2014**, *8*, 6038.
[70] Y. Xia, Z. Xiao, X. Dou, H. Huang, X. H. Lu, R. J. Yan, Y. P. Gan, W. J. Zhu, J. P. Tu, W. K. Zhang, X. Y. Tao, *Acs Nano* **2013**, *7*, 7083.
[71] B. Guo, X. Fang, B. Li, Y. Shi, C. Ouyang, Y. S. Hu, Z. Wang, G. D. Stucky, L. Chen, *Chem. Mater.* **2012**, *24*, 457.
[72] C. Liu, C. Zhang, H. Song, X. Nan, H. Fu, G. Cao, *J. Mater. Chem. A* **2016**, *4*, 3362.
[73] C. Liu, H. Song, C. Zhang, Y. Liu, C. Zhang, X. Nan, G. Cao, *Nano Res.* **2015**, *8*, 3372.
[74] F. Zhang, T. Zhang, X. Yang, L. Zhang, K. Leng, Y. Huang, Y. Chen, *Energy Environ. Sci.* **2013**, *6*, 1623.
[75] H. L. Wang, Z. W. Xu, Z. Li, K. Cui, J. Ding, A. Kohandehghan, X. H. Tan, B. Zahiri, B. C. Olsen, C. M. B. Holt, D. Mitlin, *Nano Lett.* **2014**, *14*, 1987.
[76] K. He, H. L. Xin, K. Zhao, X. Yu, D. Nordlund, T. C. Weng, J. Li, Y. Jiang, C. A. Cadigan, R. M. Richards, M. M. Doeff, X.-Q. Yang, E. A. Stach, J. Li, F. Lin, D. Su, *Nano Lett.* **2015**, *15*, 1437.
[77] C. Peng, B. Chen, Y. Qin, S. Yang, C. Li, Y. Zuo, S. Liu, J. Yang, *ACS Nano* **2012**, *6*, 1074.
[78] Z. Zhang, F. Xiao, L. Qian, J. Xiao, S. Wang, Y. Liu, *Adv. Energy Mater.* **2014**, *4*, 1400064.
[79] Z. S. Wu, W. Ren, D. W. Wang, F. Li, B. Liu, H. M. Cheng, *ACS Nano* **2010**, *4*, 5835.
[80] Y. Huang, S. L. Candelaria, Y. Li, Z. Li, J. Tian, L. Zhang, G. Cao, *J. Power Sources* **2014**, *252*, 90.
[81] X. Wang, G. Shen, *Nano Energy* **2015**, *15*, 104.
[82] A. Du Pasquier, I. Plitz, S. Menocal, G. Amatucci, *J. Power Sources* **2003**, *115*, 171.
[83] V. Ruiz, C. Blanco, R. Santamaría, J. M. Ramos-Fernández, M. Martínez-Escandell, A. Sepúlveda-Escribano, F. Rodríguez-Reinoso, *Carbon* **2009**, *47*, 195.
[84] N. Mahmood, M. Tahir, A. Mahmood, W. Yang, X. Gu, C. Cao, Y. Zhang, Y. Hou, *Sci. China Mater.* **2015**, *58*, 114.
[85] X. Yu, C. Zhan, R. Lv, Y. Bai, Y. Lin, Z.-H. Huang, W. Shen, X. Qiu, F. Kang, *Nano Energy* **2015**, *15*, 43.
[86] Q. Wang, Z. H. Wen, J. H. Li, *Adv. Funct. Mater.* **2006**, *16*, 2141.